ACS APPLIED MATERIALS & INTERFACES

Research Article

www.acsami.org

$BiFeO_3/TiO_2$ Nanotube Arrays Composite Electrode: Construction, Characterization, and Enhanced Photoelectrochemical Properties

Ashu Zhu, Qidong Zhao,* Xinyong Li, and Yong Shi

State Key Laboratory of Fine Chemicals, Key Laboratory of Industrial Ecology and Environmental Engineering (MOE), School of Environmental Science and Technology, Dalian University of Technology, Dalian 116024, China

ABSTRACT: This work aims at the exploration of nanostructured ferroelectric-material-modified semiconductor electrodes for enhanced photo-induced activity. A well-aligned $BiFeO_3/TiO_2$-nanotubes (NTs) array with visible-light activity was successfully synthesized on a titanium sheet by combining anodization and an ultrasonic-immersion method followed by annealing. The structural and optical properties of the TiO_2-NTs and the composite $BiFeO_3/TiO_2$-NTs were comparatively characterized. The composite $BiFeO_3/TiO_2$-NTs grown on a Ti sheet and used as an electrode exhibited a stronger absorption in the visible region and a much higher photoconversion efficiency than the pure TiO_2-NTs/Ti electrode. Electrochemical impedance investigation attested to a significant improvement of the interfacial electron-transfer kinetics with enhanced separation of electron-hole pairs. The as-prepared composite electrode showed a high efficiency for photoelectrocatalytic degradation towards rhodamine B under visible-light irradiation (λ > 400 nm). The enhanced photoelectrocatalytic activity of the composite electrode could be attributed to the synergistic effect between the lowered electron-hole recombination rate by the applied bias and the wider spectral response promoted by the $BiFeO_3$ component.

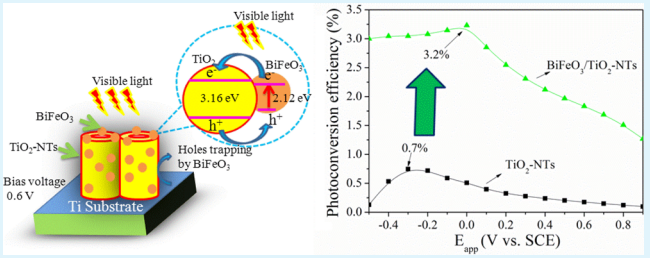

KEYWORDS: *composite electrode, nanotube arrays, photocurrent, surface photovoltage, photoelectrocatalytic activity*

INTRODUCTION

Semiconductor-based materials with advanced nanostructures have become the core element for photoconversion-related technology.[1] TiO_2 is the most investigated material in the field of solar-energy utilization because of its stability, lack of toxicity, and low cost.[2] Recently, many different nanostructures of TiO_2-based materials have been developed that have enhanced photo-induced performance.[2−5] In particular, TiO_2 nanotube arrays (TiO_2-NTs) have been regarded as one of the most promising nanostructures for photocatalysis and solar-cell applications because, compared with other TiO_2 morphologies, they have the advantages of good charge-transfer properties, high surface area, and spatially ordered dispersion. Although TiO_2-NTs-based electrodes can be conveniently prepared by anodic oxidation of Ti foil with HF electrolyte,[4−6] there are still two shortcomings for TiO_2-NTs utilized as photoelectrodes. First, an inefficient harvest of solar energy originates from its large band gap of 3.2 eV. Second, a relatively high recombination rate of the photo-induced charge carriers resides in TiO_2-NTs. Hence, many efforts have been afforded to address these two bottlenecks by doping TiO_2-NTs, for example, with nonmetals such as B−N and N−F[7−9] and metals such as Ag, Fe, Pt, and Au[10−14] or by decorating TiO_2-NTs with some narrow-band-gap semiconductors such as CdS, $ZnFe_2O_4$, β-Bi_2O_3,[15−18] and so forth. Nevertheless, further investigations addressing the shortcomings of TiO_2-NTs would be of great fundamental interest.

Recently, as a typical perovskite material, it was shown that $BiFeO_3$ exhibits both ferroelectric and magnetic polarization.[19−22] $BiFeO_3$ is also a vital visible-light-responsive photocatalyst because of its narrow band gap (E_g = 2.2−2.7 eV) and has been regarded as one of the third-generation photocatalysts.[23] Furthermore, the ferroelectric properties of the materials can help to enhance the separation efficiency of the photo-generated charges as well as their reactivity.[24] Many recent efforts have focused on promoting the photo activities of polycrystalline $BiFeO_3$ materials, such as developing powders of $BiFeO_3/TiO_2$ composites,[25,26] Gd-doped $BiFeO_3$ nanoparticles,[27] $BiFeO_3$ particles loaded with photochemically reduced Ag, and $BiFeO_3$ nanowires decorated with Au nanoparticles.[28,29] In the previous reports, $BiFeO_3$-based materials showed strong absorption of visible light and high photocatalytic performance for degrading aqueous dyes of rhodamine,[30−32] methylene blue,[33] bisphenol A,[34] and Congo red[23,26,35,36] under irradiation of visible light with wavelengths longer than 400 nm. Moreover, unassisted photocatalytic water splitting has been also achieved with $BiFeO_3$.[29,37]

In addition to the powder form of these materials, researchers have fabricated various $BiFeO_3$-based films for photoelectric devices. Unprecedentedly, Yang et al. delicately designed ordered arrays of epitaxial $BiFeO_3$ films with

Received: October 28, 2013
Accepted: December 16, 2013
Published: December 16, 2013

ACS Publications © 2013 American Chemical Society

structurally driven steps of the electrostatic potential on nanometer-scale domain walls, which could produce voltages that are significantly higher than the band gap.[38] More recently, Alexe et al. showed that by using a nanoscale top electrode, the photoexcited carriers could be efficiently collected from the $BiFeO_3$ single crystals and the external quantum efficiency was enhanced by up to seven orders of magnitude.[39] Lately, various substrates such as $Pt/TiO_2/SiO_2/Si(100)$ have been utilized to fabricate $BiFeO_3$ films for improved photoelectric devices.[40] Nevertheless, the $BiFeO_3$-based photovoltaic devices are still low in their energy-conversion efficiency compared to other narrow-band-gap semiconductors, partially because of the lack of efficient charge collection and the extremely short lifetime of a nonthermalized electron in $BiFeO_3$ bulk.[39,41]

Herein, we utilized the ordered nanostructure of TiO_2-NTs grown on a Ti sheet to enlarge the contact area with $BiFeO_3$ nanoparticles. The TiO_2-NTs behave as an efficient electrode for collecting visible-light-induced charges from excited $BiFeO_3$ nanoparticles with a smaller band gap. Simultaneously, the $BiFeO_3$ nanoparticles possess a dramatically reduced charge-collection distance for the TiO_2-NTs/Ti conjunct electrode. Furthermore, an internal spontaneous polarization of $BiFeO_3$ nanoparticles because of the pinning of the ferroelectric domains in a preferred orientation can be utilized to bend the surface-energy band of TiO_2 upward/downward at their interface, which may force the photogenerated electrons and holes to separate.[42,43] Consequently, the decreased recombination of photogenerated charge carriers would enhance the photocatalytic efficiency. In other words, the combination of $BiFeO_3$ and TiO_2-NTs may promisingly provide a better alternative to overcome the above-mentioned two deficiencies of TiO_2-NTs. It is expected that such a combination would be distinct from those modifications with nonferroelectric semiconductors.

In this work, a $BiFeO_3/TiO_2$-NTs-covered Ti electrode was fabricated by combining the anodization of a titanium sheet and an ultrasonic-immersion method followed by annealing. The morphology, crystal structure, optical properties, and photoelectrochemical performances of TiO_2-NTs and $BiFeO_3/TiO_2$-NTs grown on Ti electrodes were comparatively investigated. The photoelectrocatalytic (PEC) activities of the prepared electrodes were evaluated in the degradation of a typical dye rhodamine B (RhB) under visible-light irradiation ($\lambda > 400$ nm). It is demonstrated that the $BiFeO_3/TiO_2$-NTs-composite electrode possess significantly enhanced photoelectrochemical activity.

EXPERIMENTAL SECTION

All chemical reagents were of analytical grade and used without further purification. Electrolyte was freshly prepared from deionized water. The TiO_2-NTs were synthesized by anodic oxidation of a titanium sheet in a HF electrolyte according to a reported procedure.[6] The size of the titanium sheet was 2×4 cm^2. $BiFeO_3$ nanoparticles were deposited into TiO_2-NTs via an ultrasonic-immersion strategy, and the detailed process is described as follows. First, the $BiFeO_3$ precursor solution was prepared. In a typical procedure, 0.9701 g of bismuth nitrate and 0.8080 g of iron nitrate were dissolved in 20 mL of 2-methoxyethanol followed by the addition of 20 μL of 0.1 mol L^{-1} HNO_3 into the solution. Then, to the mixture solution was added 0.42 g of citric acid as a complexant and 10 mL of ethylene glycol as a dispersant. The mixture was stirred for 1 h at 60 °C to form a sol. Second, the TiO_2-NTs electrode was immersed vertically into the sol followed by ultrasonic processing for 1 h at 100 W power and 40 kHz frequency in a digitally controlled ultrasonic cleaner (Shumei KQ3200DB). Then, the TiO_2-NTs electrode was dried at 150 °C for 10 min. A desired deposition amount of $BiFeO_3$ sol in the TiO_2-NTs pores was obtained after three repetitions of the ultrasonic immersing in sol followed by drying at 150 °C. Finally, the $BiFeO_3/TiO_2$-NTs electrode was obtained by annealing at 500 °C for 2 h with a temperature ramp rate of 2 °C min^{-1}.

The morphology and composition of the products were characterized by scanning electron microscopy (SEM, Quanta 450) and energy-dispersive X-ray analysis (EDX, X-Max Oxford Instruments), respectively. Triangle-shaped pieces with a width of about 5 mm from each as-prepared electrode with metallic Ti substrate were cut off at the edge, which were used to obtain microscope images with the SEM instrument. The crystalline phase of the electrodes was characterized with a Shimadzu XD-3A X-ray diffractometer with Cu Kα irradiation at 30 kV and 30 mV. UV−vis diffuse-reflectance spectra (DRS) of the electrodes were collected on an UV−vis spectrophotometer (JASCO, UV-550). Surface photovoltage (SPV) spectra were obtained on a home-built measurement system, which consisted of a monochromater (model Omni-λ 3005) and a lock-in amplifier (model SR 830-DSP) with an optical chopper (model SR 540) running at a frequency of 20 Hz. ac SPV amplitude and the corresponding SPV phase spectra were recorded synchronously by the computer. To characterize the recombination behavior of the electron-hole pairs and the defect-related electronic structures in the materials, photoluminescence (PL) spectra of the electrode surface were collected using a Hitachi F-4500 (excited at λ = 325 nm) fluorescence spectrophotometer at room temperature and in an air atmosphere.

Photoelectrochemical measurements were conducted with a three-electrode electrolyzer system and a CHI760c (CHI Co.) electrochemical workstation. The TiO_2-NTs grown on a Ti sheet (2×4 cm^2) and $BiFeO_3/TiO_2$-NTs with metallic Ti substrate (2×4 cm^2) were studied as the working electrodes. At the same time, a saturated calomel electrode (SCE) and Pt foil (2×4 cm^2) served as the reference electrode and the counter electrode, respectively. The working electrode was irradiated with visible light ($\lambda > 400$ nm) through a UV-cutoff filter (Shanghai Seagull Colored Optical Glass Co., Ltd.) from a high-pressure xenon short arc lamp (a Phillips 500 W Xe lamp); the light intensity was 140 mW cm^{-2}, which was measured by an FZ-A irradiatometer (Photoelectric Instrument Factory of Beijing Normal University, capable of measuring the wavelength range of 400−1000 nm). Electrochemical impedance spectroscopy (EIS) was taken at a frequency range from 10^{-2} to 10^5 Hz and under an initial potential of 0.3 V. The electrolyte for the photoelectron current and EIS was 0.01 mol L^{-1} Na_2SO_4 solution.

The PEC activity of the composite electrode was tested by degradation of RhB, which was carried out in a quartz reactor. All experiments used a 0.01 M Na_2SO_4 solution as the electrolyte and were accompanied with magnetic stirring. The initial concentration of the RhB aqueous solution was 20 mg L^{-1} during the experiment. A 500 W Xe lamp with a UV-cutoff filter ($\lambda > 400$ nm) was used as the visible-light source. Upon illumination for every half an hour, 3 mL of the reaction solution was extracted and analyzed by recording UV−vis spectra on a UV 1100 spectrophotometer. The concentration of RhB was determined at its characteristic absorption wavelength of 554 nm.

RESULTS AND DISCUSSION

Figure 1 shows the XRD patterns for the JCPDS data reference (curves i, iii, and v), blank Ti sheet substrate (curve ii), TiO_2-NTs grown on Ti substrate (curve iv), and $BiFeO_3/TiO_2$-NTs (curve vi), which was also grown on a Ti substrate. From curve ii, the main diffraction peaks of the Ti sheet are observed at about 2θ = 35.2°, 38.5°, 40.3°, and 53.2°. The peaks can be indexed to the (100), (002), (101), and (102) crystalline planes of the hexagonal phase of metallic Ti (JCPDS no. 05-0682), respectively.[16] By comparison, in curve iv for the TiO_2-NTs with the Ti substrate, two more peaks at 2θ = 25.2° and 48.2° correspond to the tetragonal phase of anatase TiO_2 (101) and (200) facets, respectively. The peak of the (101) crystalline

dx.doi.org/10.1021/am404774z | ACS Appl. Mater. Interfaces 2014, 6, 671−679

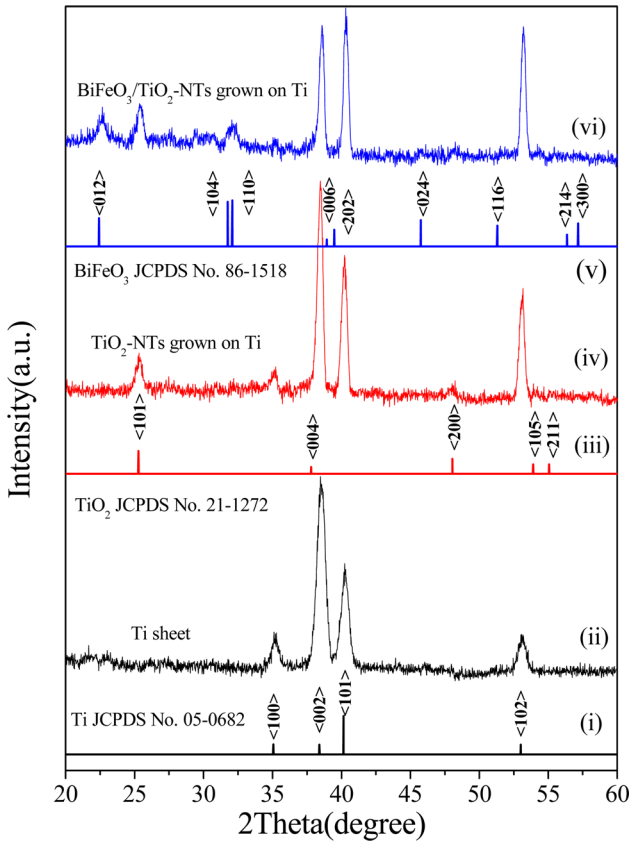

Figure 1. X-ray diffraction patterns of the reference peaks of Ti metal (JCPDS no. 05-0682) (i), Ti sheet (ii), the reference peaks of anatase TiO_2 (JCPDS no. 21-1272) (iii), TiO_2-NTs with Ti substrate (iv), the reference peaks of $BiFeO_3$ (JCPDS no. 86-1518) (v), and $BiFeO_3$/TiO_2-NTs with Ti substrate (vi).

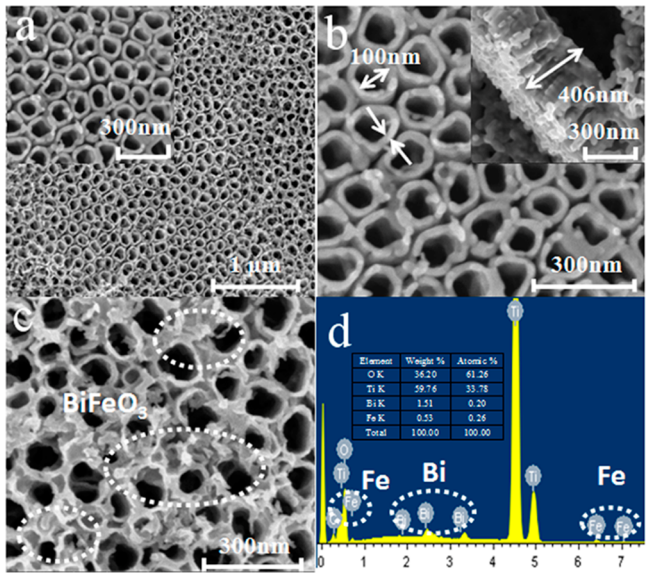

Figure 2. (a) Top-view SEM images of the TiO_2-NTs. The inset shows the images of TiO_2-NTs at high magnification. (b) Top-view SEM images of the TiO_2-NTs at high magnification. The inset shows the side-view SEM images of the TiO_2-NTs. (c) Top-view SEM images of the $BiFeO_3$/TiO_2-NTs. (d) EDX pattern of a sample of $BiFeO_3$/TiO_2-NTs. The inset shows the apparent weight and atomic percentage of each element.

plane at $2\theta = 25.2°$ indicates a preferential growth of the TiO_2-NTs along the (101) facet direction. For $BiFeO_3$/TiO_2-NTs on Ti substrate, curve vi, three more diffraction peaks appear at $2\theta = 22.6°$, 31.7°, and 32.1° in addition to those belonging to the Ti sheet and TiO_2-NTs peaks. They could be attributed to $BiFeO_3$ loaded onto TiO_2-NTs and indexed to the (012), (104), and (110) crystalline planes of the hexagonal phase of $BiFeO_3$ (JCPDS no. 86-1518), respectively, whereas the cell parameters of the prepared $BiFeO_3$ are tentatively estimated as $a = 0.5579$ and $c = 1.387$ nm by referencing the JCPDS file.

Figure 2 shows the local SEM images of TiO_2-NTs (Figure 2a,b) and the $BiFeO_3$/TiO_2-NTs (Figure 2c) of some 5 mm cut-off parts from the as-prepared electrodes as well as the EDX spectrum for the composite electrode (Figure 2d). From the top view of TiO_2-NTs in Figure 2a, the nanotubes are well-ordered and tight, and the surface is relatively smooth. In addition, the average length of the nanotube is about 406 nm, and the average pore diameter is about 100 nm. The wall thickness is around 30 nm. After loading $BiFeO_3$ nanoparticles onto the TiO_2-NTs, additional nanoparticles appeared at the interstitial space between nanotubes and around the surface edge of the TiO_2-NTs walls, with a certain amount of them having penetrated into the TiO_2-NTs pores. The morphology of the TiO_2-NTs structure still maintains its integrity, and there is no obvious change in its size (Figure 2c). This observation indicates that the loading process did not damage the ordered TiO_2-NTs array structures. The EDX spectrum in Figure 2d further proves the successful preparation of $BiFeO_3$-loaded TiO_2-NTs. The EDX data of the $BiFeO_3$/TiO_2-NTs composite indicate that the sample is composed of Ti, O, Bi, and Fe elements, with an apparent atomic ratio of Bi and Fe of about 0.8:1.

Figure 3a shows the UV−vis absorption spectra recorded from the pure TiO_2-NTs and the $BiFeO_3$/TiO_2-NTs grown on Ti sheets. Besides the super band-gap absorption of anatase below 388 nm, two more weak peaks are observed for TiO_2-NTs in the spectra in Figure 3a. The hole traps with electrons occupied show an absorption band centered at around $\lambda = 430$ nm (photon energy of 2.88 eV), whereas the deep electron traps exhibit another absorption band at $\lambda > 500$ nm centered at 580 nm (2.14 eV), which is correlated with the sub-band-gap states of the TiO_2-NTs.[44,45] These spectra indicate that the TiO_2-NTs absorbed mainly UV light, whereas the absorption edge of the $BiFeO_3$/TiO_2-NTs extended to a visible wavelength of 550 nm.

The band-gap energies of the two photo-active components can be estimated from Tauc's plots by $(\alpha h\nu) = A(h\nu - E_g)^{n/2}$, where α is the absorption coefficient near the absorption edge, h is Planck's constant, A is a constant, ν is the light frequency, E_g is the absorption band-gap energy, and n is 1 and 4 for a direct- and indirect-band-gap semiconductor, respectively.[23,46] Plots of $(\alpha h\nu)^2$ versus $h\nu$ of the samples are show in Figure 3b,c. This relationship gives E_g by estimating the straight portion of the $(\alpha h\nu)^2$ versus $h\nu$ plot to $\alpha = 0$. The band gap of TiO_2-NTs is estimated to be about 3.16 eV.[47] Because $BiFeO_3$ nanoparticles are loaded on TiO_2-NTs, the absorbance value of $BiFeO_3$ is extrapolated from the absorbance of $BiFeO_3$/TiO_2-NTs minus the background value of TiO_2-NTs, whereas the band gap of $BiFeO_3$ on TiO_2-NTs is estimated to be about 2.12 eV.[48] The UV−vis spectral variation suggests that the loading of $BiFeO_3$ significantly enhanced the visible-light absorption of TiO_2-NTs.

dx.doi.org/10.1021/am404774z | ACS Appl. Mater. Interfaces 2014, 6, 671−679

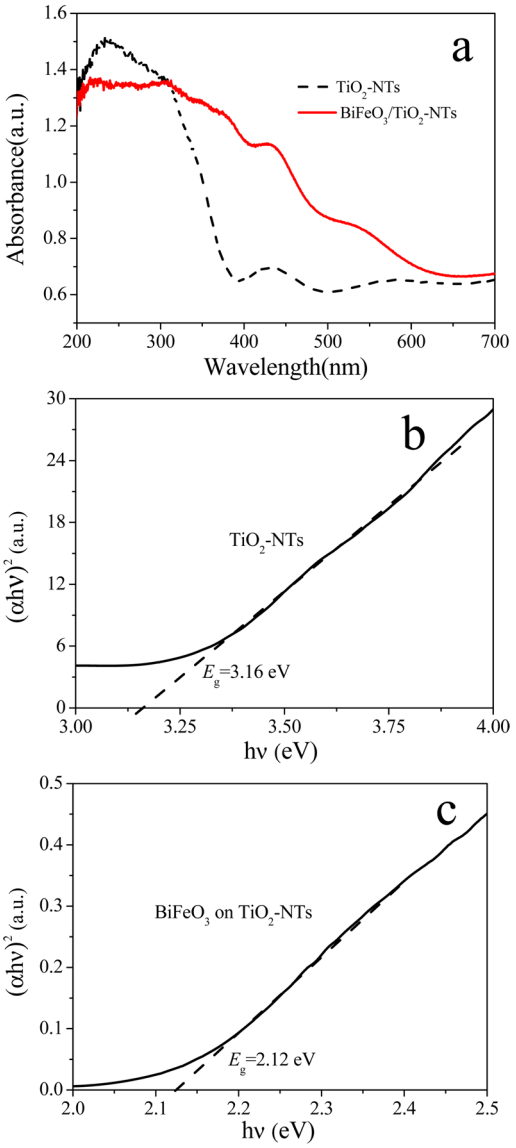

Figure 3. (a) UV−vis DRS of the TiO_2-NTs and $BiFeO_3/TiO_2$-NTs grown on Ti sheets. (b, c) Tauc's plots to determine the band gaps for TiO_2-NTs and $BiFeO_3$ on TiO_2-NTs.

SPV spectroscopy effectively disclosed the separation properties of photo-generated charge carriers under monochromic excitation on the spectrum. Generally, a stronger SPV response implies a higher separation efficiency of photo-induced charges in the illuminated system. Figure 4a reveals the ac SPV amplitude spectra of TiO_2-NTs and $BiFeO_3/TiO_2$-NTs. For $BiFeO_3/TiO_2$-NTs, an SPV response ranging from 450 to 300 nm was obtained, which is much broader than that of TiO_2-NTs. Although from 345 to 300 nm the SPV response of $BiFeO_3/TiO_2$-NTs is comparable to pure TiO_2-NTs, the SPV amplitude of $BiFeO_3/TiO_2$-NTs at 350 nm and the longer wavelengths toward the visible region are significantly higher than TiO_2-NTs. The enhanced SPV amplitude indicates that the modification of $BiFeO_3$ nanoparticles successfully extended the spectral-response range of TiO_2-NTs for improved utilization of visible light.

The SPV results are consistent with the analysis of the DRS characterization, and the difference between them originates from the nature of the SPV response in that an SPV signal is caused by the effective spatial separation of photo-induced electrons from the holes beyond light absorption. The SPV spectral edge of $BiFeO_3/TiO_2$-NTs exactly revealed an effective band-gap energy of 2.7 eV to distinguish photo-induced electron transfer. By a combination of the SPV amplitude spectra in Figure 4a and the corresponding phase values (−50 to 0°) in Figure 4b, we can conclude that the SPV response is positive for both samples, which reveals that upon illumination the photo-induced holes accumulate at the TiO_2-NTs surface and the excess electrons tend to transfer along the nanotubes towards the Ti substrate.[49] For the spectral region above 450 nm, the SPV phase data of the two samples run randomly without definite SPV amplitude values.

The positive SPV response above 400 nm for the $BiFeO_3$ loaded onto the TiO_2-NTs surface unambiguously indicates that the photo-induced electrons generated within $BiFeO_3$ nanoparticles can be effectively injected into the TiO_2-NTs. The enhanced photovoltage might be correlated with the ferroelectric properties of $BiFeO_3$. Upon loading $BiFeO_3$, electric polarization could be induced by the ferroelectric $BiFeO_3$ nanoparticles located at the interface between TiO_2 and $BiFeO_3$.[43] The surface band bending of TiO_2 nanotubes will be enhanced at the contact with $BiFeO_3$. Then, the photo-induced surface-charge recombination may decrease in TiO_2-NTs once the excess holes and electrons are produced therein.

The PL spectrum is closely related to the recombination of excited electrons and holes, which can be utilized to reveal the electronic-transition-correlated energy levels. Herein, room-temperature PL spectra were measured in air at an excitation

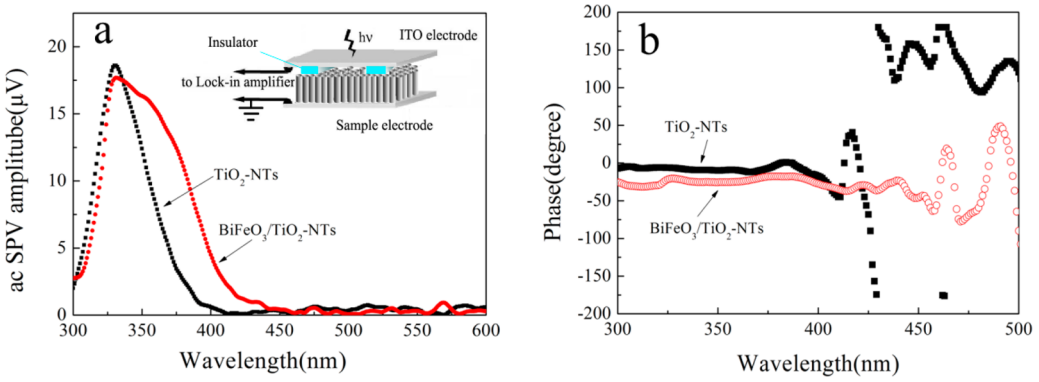

Figure 4. (a) SPV amplitude spectra for the TiO_2-NTs and $BiFeO_3/TiO_2$-NTs grown on Ti sheets. Inset: schematic of ac SPV measurement configurations for the samples. (b) Corresponding phase spectra for TiO_2-NTs and $BiFeO_3/TiO_2$-NTs.

dx.doi.org/10.1021/am404774z | ACS Appl. Mater. Interfaces 2014, 6, 671−679

wavelength of 325 nm. The UV irradiation at 325 nm will produce some hot electrons that relax to the bottom of the conduction band where their mobility enables them to reach certain defect sites or elsewhere. Trapped charge carriers can recombine at such defect sites that lie within the band gap, emitting photons with a spectrum of energies. The PL spectra in Figure 5 show that the shapes of the PL spectra are similar

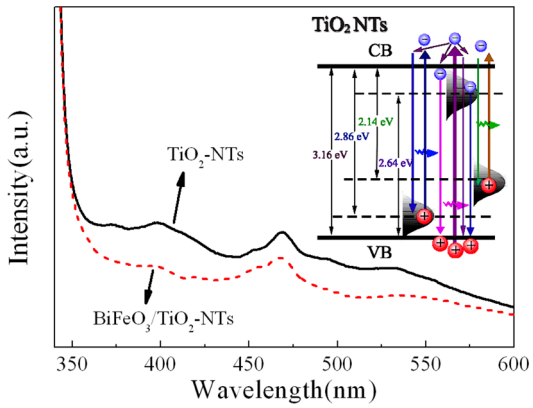

Figure 5. PL spectra of the TiO_2-NTs and $BiFeO_3/TiO_2$-NTs grown on a Ti substrate excited by photons at 325 nm. Inset: schematic of the multiple charge-generation and relaxation pathways of excited electrons and holes related to the defect states and energy bands in which the energy values are calculated from the spectral peaks of the DRS and PL spectra of TiO_2-NTs. The shape of the minus sign in the circle denotes the excited electron, and the plus sign in the circle denotes the hole. VB and CB denote the valence band and conduction band of TiO_2, respectively.

for both electrodes, indicating the dominant role of TiO_2-NTs in PL generation. By contrast, the pure TiO_2-NTs exhibit a higher emission intensity than $BiFeO_3/TiO_2$-NTs. The decrease of the emission intensity is indicative of a decrease in the irradiative recombination of the charges for the $BiFeO_3$-modified TiO_2-NTs. Some typical emission peaks appear at 400 (3.1 eV), 467 (2.64 eV), and 535 nm (2.32 eV). Herein, the PL signal at 400 nm can be attributed to band-edge emission of free excitons. A strong 467 nm luminescence peak may be caused by the surface-states related recombination of the electron-hole pairs in TiO_2-NTs. The green photoluminescence of anatase around 535 nm might be assigned to the recombination of conduction-band electrons with deeply trapped holes at the oxygen vacancies of TiO_2-NTs.[45,50]

By summing the DRS and PL spectra, the inset of Figure 5 was added for understanding better some of the typical transition pathways related to the surface states in the TiO_2-NTs. Above the valence band top, shallow and deep traps for holes caused by oxygen vacancies may coexist in TiO_2-NTs as electron-acceptor-type defects. Electron-donor-type defects, such as Ti^{3+} sites, form the shallow energy states near the conduction band bottom. After excitation, some mobile electrons may transfer and be trapped at the shallow energy states within the band gap, which could subsequently emit blue photons by recombination with the holes in valence band. The emissive hole traps could be ascribed to oxygen vacancy color centers, which could also lead to the absorption band around a blue wavelength of 434 nm (2.86 eV).[45]

The photoelectrochemical performance of the TiO_2-NTs and $BiFeO_3/TiO_2$-NTs grown on a Ti substrate were investigated under visible-light irradiation (500 W Xe lamp, 140 mW cm^{-2}).

The photocurrent densities as a function of the applied potential of the electrodes in a 0.01 M Na_2SO_4 solution are presented in Figure 6a. The dark current densities were found

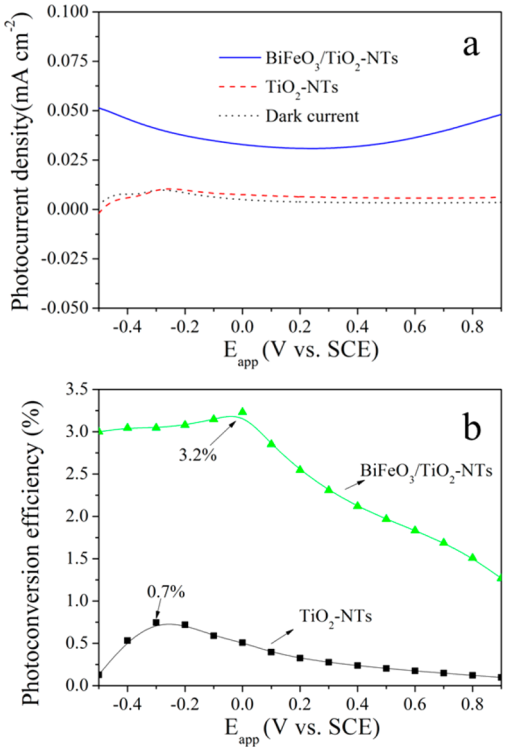

Figure 6. (a) Variation of photocurrent density vs bias potential (vs SCE) and (b) photoconversion efficiency as a function of applied potential (vs SCE) in a 0.01 M Na_2SO_4 solution for the $BiFeO_3/TiO_2$-NTs and TiO_2-NTs electrodes under visible-light irradiation (140 mW cm^{-2}).

to be negligible. However, when the visible light was on, the saturated photocurrent density of the $BiFeO_3/TiO_2$-NTs electrode was about 8.3-fold as high as that of the TiO_2-NTs. From this, we can conclude that the $BiFeO_3/TiO_2$-NTs composite has a much higher conversion capability of visible light and that the photo-generated carrier-separation efficiency is improved significantly after the modification by $BiFeO_3$.

The photoconversion efficiency (η) of light energy to chemical energy in the presence of a bias potential is calculated as[51]

$$\eta\ (\%) = [(\text{total power output} - \text{electrical power input})/\text{light power input}]100 = [j_p(E^0_{rev} - |E_{app}|)100]/I_0$$

where j_p is the photocurrent density (mA cm^{-2}), $j_pE^0_{rev}$ is the total power output, $j_p|E_{app}|$ is the electrical power input, and I_0 is the power density of the incident light (mA cm^{-2}). E^0_{rev} is the standard reversible potential (which is 1.23 V for the water-splitting reaction at pH 0), and $|E_{app}|$ is the absolute value of the applied potential E_{app}, which is obtained as $E_{app} = E_{meas} - E_{aoc}$, where E_{meas} is the electrode potential (vs SCE) of the working electrode at which the photocurrent is measured under illumination and E_{aoc} is the electrode potential (vs SCE) of the same working electrode under open-circuit conditions, under the same illumination, and in the same electrolyte.

dx.doi.org/10.1021/am404774z | ACS Appl. Mater. Interfaces 2014, 6, 671−679

Figure 6b shows the total percent photoconversion efficiency (η_{photo} (total), %) as a function of the applied potential (E_{app} (V) vs SCE) for the $BiFeO_3/TiO_2$-NTs and TiO_2-NTs. The maximum photoconversion efficiency is 3.2% for $BiFeO_3/TiO_2$-NTs, whereas it was only 0.7% for TiO_2-NTs. The significant photocurrent and efficiency achieved herein show that the composite $BiFeO_3/TiO_2$-NTs electrode promotes enhanced photoelectrochemical performance under visible light, which is much higher than the previously reported $ZnFe_2O_4/TiO_2$-NTs electrode.[16]

To investigate the photoelectric properties of the TiO_2-NTs and $BiFeO_3/TiO_2$-NTs composite further, we compared the electrochemical impedance spectra of TiO_2-NTs and $BiFeO_3/TiO_2$-NTs under dark and visible-light irradiation conditions (Figure 7). In the dark, the impedance arcs of the two

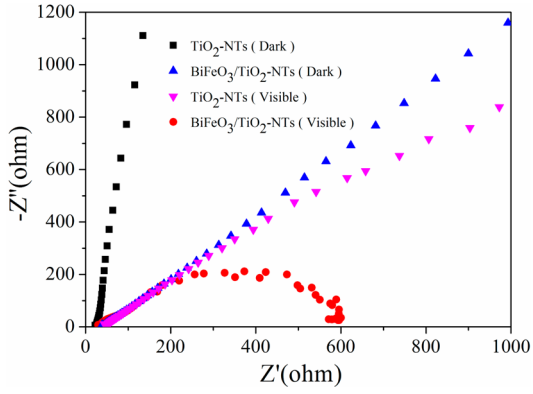

Figure 7. EIS Nyquist plots of the TiO_2-NTs and $BiFeO_3/TiO_2$-NTs electrodes in the dark and under visible-light irradiation (λ > 400 nm, I_0 = 140 mW cm^{-2}). The bias potential is 0.3 V (vs SCE).

electrodes are large, indicating that the electrons going through the electrode and electrolyte interface are few. In general, a smaller radius of the arc on the EIS Nyquist plot means that the charge-transfer speed is faster.[4] The radius of the arc on the EIS Nyquist plot of $BiFeO_3/TiO_2$-NTs is smaller than that of TiO_2-NTs, which indicates that the charge-transfer resistance decreases after the deposition of $BiFeO_3$ nanoparticles. The decrease in resistance may reveal the increased charge-transfer path across the electrode surface layer of $BiFeO_3/TiO_2$-NTs to the Ti substrate. Under visible-light irradiation, the arc radius on the EIS Nyquist plot of $BiFeO_3/TiO_2$-NTs is smaller than that of TiO_2-NTs. The difference in EIS Nyquist plots confirms that the loading of $BiFeO_3$ increases the photogenerated charge carriers and accelerates the photogenerated charges transfer between the composite electrode and electrolyte interface.

To evaluate the PEC activity of the $BiFeO_3/TiO_2$-NTs electrode, PEC experiments for RhB degradation were carried out under visible-light irradiation (140 mW cm^{-2}). The RhB was decolored in different degradation processes, that is, the PEC process, the photocatalytic process, the electrochemical (EC) process, and the direct photolysis (DP), as presented in Figure 8. For comparison, the PEC degradation of RhB using TiO_2-NTs was also performed. In addition, the applied bias voltage on the photo-active electrode for the PEC and EC processes was 0.6 V. Figure 8a displays the absorption spectra of an RhB aqueous solution at different times during the PEC process with $BiFeO_3/TiO_2$-NTs as the photo anode. With visible-light irradiation, the absorption peaks at λ = 554 nm gradually diminished during the PEC process. The hypsochro-

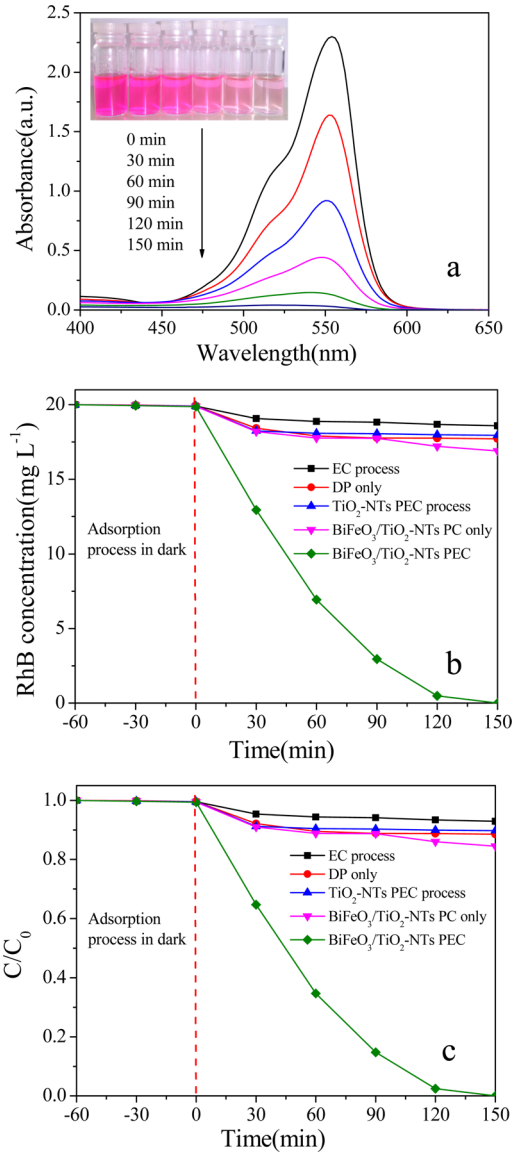

Figure 8. (a) UV−vis spectra of an RhB solution by PEC treatment with $BiFeO_3/TiO_2$-NTs electrode under visible-light irradiation (I_0 = 140 mW cm^{-2}, 0.6 V vs SCE bias potential). The inset shows photographs of the color change of the RhB solution during different reaction times. (b) RhB concentration varying with time through different degradation processes. (c) Ratio of degraded RhB varying with treatment time, where C_0 is the initial concentration of RhB (C_0 = 20 mg/L) and C is the RhB concentration after a certain treatment time. PC denotes a photocatalytic process.

mic shifts of the absorption band of RhB are insignificant. It is supposed that deethylation is negligible and that the cleavage of the whole chromophore structure (cycloreversion) of RhB happens preferentially over the electrode surface.[52] In 150 min of degradation, the absorption intensity of RhB for the characteristic peak at λ = 554 nm is close to 0. This result is also consistent with the gradual color change of the reaction solution from red to almost colorless during the different reaction times (Figure 8a, inset).

Combining Figure 8, panels b and c, all of the adsorption processes in the dark have no effect on the mineralization of RhB. The RhB was almost completely degraded by the PEC process in 150 min, whereas only 7, 12, and 16% of the RhB removal were obtained in the EC, DP, and photocatalytic

dx.doi.org/10.1021/am404774z | ACS Appl. Mater. Interfaces 2014, 6, 671−679

processes with the same illumination time, respectively. The PEC process has the best degradation efficiency among these processes. Compared to the $BiFeO_3/TiO_2$-NTs electrode, the TiO_2-NTs degraded only 10% of the RhB during the same time in the PEC process.

The degradation of RhB by the EC, DP, photocatalytic, and PEC processes were all found to follow the pseudo-first-order-decay kinetics. One can use the Langmuir–Hinshelwood model to simulate this,[53] and the reaction rate equation is

$$\ln(C_0/C_t) = kt$$

where C_0 is the initial concentration of RhB (C_0 = 20 mg/L), t is the illumination time, C_t is the RhB concentration after irradiation for t min, and k is the first-order kinetic constant. The values of k and regression coefficient (r^2) are listed in Table 1. From Table 1, the k value of the PEC process using

Table 1. Kinetic Constants and Regression Coefficients for RhB Degradation Using Different Processes under Visible-Light Irradiation

sample	process	kinetic constant (min^{-1})	r^2
$BiFeO_3/TiO_2$-NTs	EC	1×10^{-4}	0.9250
	DP	3×10^{-4}	0.7206
	photocatalytic	6×10^{-4}	0.9560
	PEC	2×10^{-2}	0.9788
TiO_2-NTs	PEC	2×10^{-4}	0.9764

the $BiFeO_3/TiO_2$-NTs electrode is the largest among the various methods. It is also shown that the degradation efficiency of the PEC process using $BiFeO_3/TiO_2$-NTs is significantly higher than that of TiO_2-NTs. The improvement is partially because the composite electrode has a lower recombination rate of electrode-hole pairs; meanwhile, the $BiFeO_3$ component significantly enhances the spectral response of the electrode.

Herein, one may raise the question of why the photocatalytic performance of the composite electrode is as low as the pure TiO_2-NTs electrode without applied external bias, whereas a much higher surface photovoltage in the visible spectral region was observed with $BiFeO_3$ loading. Considering the rule for an effective photocatalytic reaction and the low efficiency of the TiO_2-NTs electrode under visible light, one possible explanation is the absence of effective separation of photo-induced charges by the electrolyte-soaked composite system. Higher upward surface-band bending in TiO_2-NTs might be induced by the contact electrolyte, causing mismatched interfacial energy bands between TiO_2-NTs and $BiFeO_3$. The interfacial potential barrier would hinder the excess electrons generated by $BiFeO_3$ from transferring to TiO_2-NTs, whereas a properly applied positive bias could help to lower the barrier and to facilitate the charge transfer between $BiFeO_3$ and TiO_2-NTs. Another plausible mechanism is help from the applied positive bias to drive the transfer of photo-induced electrons from $BiFeO_3$ to TiO_2-NTs, where the holes would be left on the $BiFeO_3$ for a subsequent oxidative reaction.

The stability and recyclability of the $BiFeO_3/TiO_2$-NTs electrode was evaluated by repeating RhB degradation under visible-light illumination five times. The composite array electrode was cleaned with proper ultrasonication after each experiment under the same conditions. As shown in Figure 9, the degradation efficiencies of RhB for the five cycles are 100, 99, 99, 98, and 97%, respectively. There is no obvious decline in the PEC activity of $BiFeO_3/TiO_2$-NTs in the degradation of

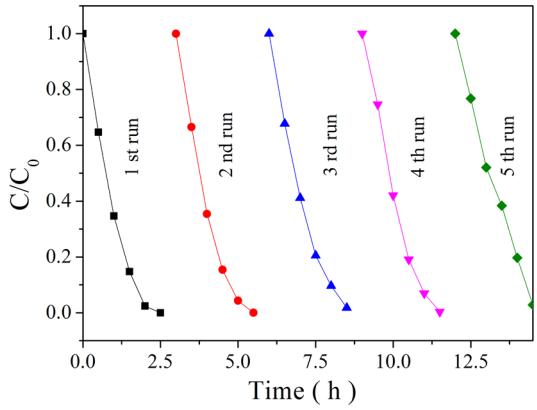

Figure 9. PEC degradation of RhB by the $BiFeO_3/TiO_2$-NTs electrode for five cycles.

RhB after five recycles. Therefore, the $BiFeO_3/TiO_2$-NTs electrode is fairly stable and can be reused without a significant loss of activity.

A cartoon diagram of the photo-generated charge generation, separation, and transfer path over the $BiFeO_3/TiO_2$-NTs electrode is shown in Figure 10a. It is well-known that during photocatalysis the substrate adsorption, light absorption by the photocatalyst, and charge generation and separation are crucial factors in determining the reactivity. The phenomenon of RhB adsorption by the electrodes is not very distinct because of the limited volume and amount of TiO_2-NTs, as evidenced by the adsorption experiment (Figure 8). The TiO_2-NTs band-gap energy is estimated to be 3.16 eV by considering its response edges from the DRS spectra in Figure 3b, and it is active only under UV irradiation. Because $BiFeO_3$ is a narrow-band-gap semiconductor with E_g = 2.12 eV (extrapolated from Figure 3c),[23] it may be excited by certain wavelengths of visible light (400 nm < λ < 585 nm), although the actual upper-limit wavelength for effective excitation to generate excess charges should be around 460 nm according to the SPV spectra, corresponding to an effective band-gap energy of 2.7 eV. Upon effective excitation, many photo-induced electron-hole pairs would be dissociated into charge carriers because of the internal ferroelectric polarization of $BiFeO_3$ nanoparticles.

The conduction band, valence band, and Fermi level positions of independent n-type TiO_2[53−56] and $BiFeO_3$[26,57−61] are summarized from previous reports in Figure 10b. n-Type conduction is assumed for the prepared $BiFeO_3$ nanoparticles. When the composite material, $BiFeO_3/TiO_2$-NTs, is formed, the system has to reach thermal equilibrium, which means the Fermi levels of the two materials would achieve consistency. Although the conduction-band potential of TiO_2 may be a little more cathodic than that of $BiFeO_3$, which is unfavorable for effective charge separation between them, the photo-generated electrons can be forced to transfer from the conduction band of $BiFeO_3$ to TiO_2 under an applied bias potential of 0.6 V, which would significantly help to reduce the charge recombination within the $BiFeO_3$ nanoparticles, whereas the holes would spontaneously transfer from TiO_2-NTs to $BiFeO_3$, subsequently participating in the reaction with RhB.

The separated, photo-generated electrons can react with the surface chemisorbed O_2 to generate the strong oxidative species $O_2^{\bullet-}$, which combines with H^+ from solution to form H_2O_2. Finally, accumulated electrons in the counter electrode can react with H_2O_2 to generate $^{\bullet}OH$, which would play an

dx.doi.org/10.1021/am404774z | ACS Appl. Mater. Interfaces 2014, 6, 671−679

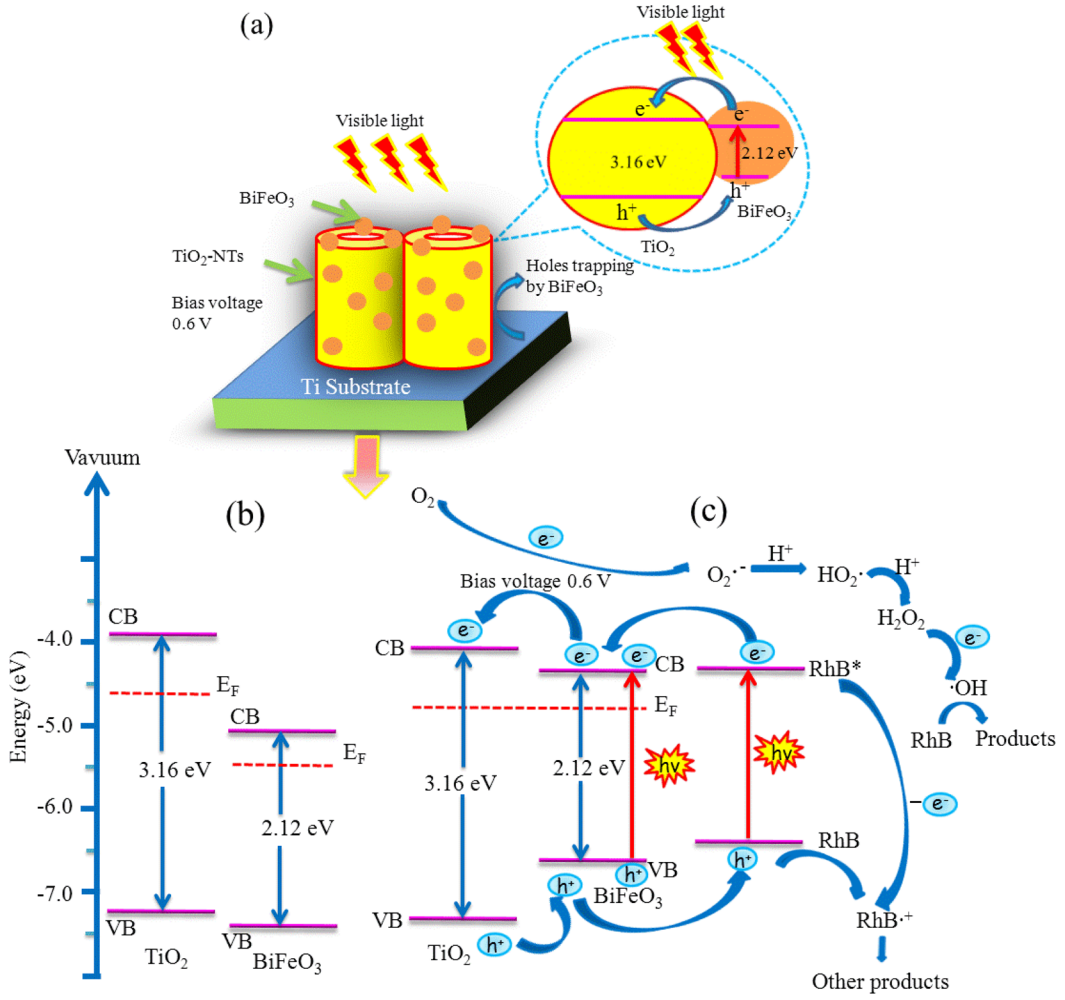

Figure 10. (a) Cartoon diagram of the photo-generated electron generation, separation, and transfer path in $BiFeO_3/TiO_2$-NTs upon visible-light excitation. (b) Conduction band, valence band, and Fermi level positions of independent n-type TiO_2 and n-type $BiFeO_3$. (c) Schematic pathways of PEC degradation of RhB over $BiFeO_3/TiO_2$-NTs under a bias of 0.6 V applied onto the composite electrode.

important role in degrading and mineralizing the adsorbed molecules of RhB nearby.[62,63] The holes can also react with surface-adsorbed H_2O to produce $^{\bullet}OH$ radicals or directly oxidize the adsorbed RhB molecules into their radicals. Meanwhile, RhB molecules could also be excited directly by the visible-light irradiation, leading to the generation of certain organic radicals, which is known as a self-sensitization mechanism.[64,65] During such a process, other active oxidizing species could also be formed, which would be involved in the self-sensitized photo-degradation of RhB. On the basis of the above results and previous reports,[66,67] we propose the mechanisms of light absorption, charge transfer, and the reaction pathways for generating active radicals by the $BiFeO_3/TiO_2$-NTs electrode and the degradation of RhB in Figure 10c.

CONCLUSIONS

The surface modification by $BiFeO_3$ nanoparticles remarkably improves the surface photovoltage and photochemical responses of TiO_2-NTs because of significantly enhanced visible-light utilization. Furthermore, the $BiFeO_3/TiO_2$-NTs composite electrode exhibits much greater PEC activity for RhB degradation under visible-light irradiation. The $BiFeO_3$ component plays a key role in promoting the generation of photo-induced charges under visible light. A proper positive bias applied onto the composite electrode could greatly enhance its photochemical performance, which may be related to the ferroelectric properties of polarized $BiFeO_3$ nanoparticles. Such a composite system could also be utilized in other catalytic reactions driven by visible light. It is expected that further optimizing the ordering of the ferroelectric domain walls in the $BiFeO_3$ nanoparticles with respect to the oriented TiO_2 nanotubes will lead to a higher photoelectric performance of the composite electrode.

AUTHOR INFORMATION

Corresponding Author

*E-mail: zhaoqidong@dlut.edu.cn.

Author Contributions

The manuscript was written through contributions of all authors. All authors have given approval to the final version of the manuscript.

Notes

The authors declare no competing financial interest.

ACKNOWLEDGMENTS

This work was supported by the National Nature Science Foundation of China (nos. 21207015 and NSFC-RGC 21061160495), the Major State Basic Research Development

Program of China (973 Program) (no. 2011CB936002), and the Key Laboratory of Industrial Ecology and Environmental Engineering, China Ministry of Education. A.Z. appreciates the 123 Project of Liaoning (environmental education research) supported by Geping Green. We are most grateful to the reviewers for their constructive comments.

REFERENCES

(1) Wang, R.; Hashimoto, K. *Nature* **1997**, *388*, 431−432.
(2) Chen, X. B.; Samuel, S. M. *Chem. Rev.* **2007**, *107*, 2891−2959.
(3) Zheng, X.; Kuang, Q.; Yan, K.; Qiu, Y.; Qiu, J.; Yang, S. *ACS Appl. Mater. Interfaces* **2013**, *5*, 11249−11257.
(4) Zhang, Z.; Yu, Y.; Wang, P. *ACS Appl. Mater. Interfaces* **2012**, *4*, 990−996.
(5) Zhang, Q.; Xu, H.; Yan, W. *Nanosci. Nanotechnol. Lett.* **2012**, *4*, 505−519.
(6) Hou, Y.; Li, X.; Zhao, Q.; Chen, G.; Rasto, C. L. *Environ. Sci. Technol.* **2012**, *46*, 4042−4050.
(7) Zhou, X.; Peng, F.; Wang, H.; Yu, H.; Yang, J. *Electrochem. Commun.* **2011**, *13*, 121−124.
(8) Su, Y.; Zhang, X.; Zhou, M.; Han, S.; Lei, L. *J. Photochem. Photobiol., A* **2008**, *194*, 152−160.
(9) Lei, L.; Su, Y.; Zhou, M.; Zhang, X.; Chen, X. *Mater. Res. Bull.* **2007**, *42*, 2230−2236.
(10) Li, X.; Zou, X.; Qu, Z.; Zhao, Q.; Wang, L. *Chemosphere* **2011**, *83*, 674−679.
(11) Sun, L.; Li, J.; Wang, C.; Li, S.; Lai, Y.; Chen, H.; Lin, C. *J. Hazard. Mater.* **2009**, *171*, 1045−1050.
(12) Wu, Q.; Ouyang, J.; Xie, K.; Sun, L.; Wang, M.; Lin, C. *J. Hazard. Mater.* **2012**, *199-200*, 410−417.
(13) Andrei, H.; Mathias, L.; Sergiu, A.; Max, A.; Marek, S.; Robert, L.; Patrik, S.; Joerg, L. *J. Phys. Chem. C* **2010**, *114*, 20146−20154.
(14) Yang, L. X.; Yang, W. Y.; Cai, Q. Y. *J. Phys. Chem. C* **2007**, *111*, 16613−16617.
(15) Shao, Z.; Zhu, W.; Li, Z.; Yang, Q.; Wang, G. *J. Phys. Chem. C* **2012**, *116*, 2438−2442.
(16) Hou, Y.; Li, X. Y.; Zhao, Q. D.; Quan, X.; Chen, G. H. *Adv. Funct. Mater.* **2010**, *20*, 2165−2174.
(17) Natarajan, T. S.; Natarajan, K.; Bajaj, H. C.; Tayade, R. J. *J. Nanopart. Res.* **2013**, *15*, 1669.
(18) Li, D.; Zhang, Y.; Zhang, Y.; Zhou, X.; Guo, S. *J. Hazard. Mater.* **2013**, *258-259*, 42−49.
(19) Zou, X.; You, L.; Chen, W. G.; Ding, H.; Wu, D.; Wu, T.; Chen, L.; Wang, J. L. *ACS Nano* **2012**, *6*, 8997−9004.
(20) Moubah, R.; Rousseau, O.; Colson, D.; Artemenko, A.; Maglione, M.; Viret, M. *Adv. Funct. Mater.* **2012**, *22*, 4814−4818.
(21) Zhang, J.; Su, X.; Shen, M.; Dai, Z.; Zhang, L.; He, X.; Cheng, W.; Cao, M.; Zou, G. *Sci. Rep.* **2013**, *3*, 2109.
(22) Zou, X.; You, L.; Chen, W. G.; Ding, H.; Wu, D.; Wu, T.; Chen, L.; Wang, J. L. *ACS Nano* **2012**, *6*, 8997−9004.
(23) Li, S.; Lin, Y. H.; Zhang, B. P.; Wang, Y.; Nan, C. W. *J. Phys. Chem. C* **2010**, *114*, 2903−2908.
(24) Safi, R.; Shokrollahi, H. *Prog. Solid State Chem.* **2012**, *40*, 6−15.
(25) Zhang, Y.; Schultz, A. M.; Li, L.; Chien, H.; Salvador, P. A.; Rohrer, G. S. *Acta Mater.* **2012**, *60*, 6486−6493.
(26) Li, S.; Lin, Y.-H.; Zhang, B.-P.; Li, J. F.; Nan, C.-W. *J. Appl. Phys.* **2009**, *105*, 054310-1−054310-5.
(27) Lotey, G. S.; Verma, N. K. *Chem. Phys. Lett.* **2013**, *574*, 71−77.
(28) Schultz, A. M.; Zhang, Y.; Salvador, P. A.; Rohrer, G. S. *ACS Appl. Mater. Interfaces* **2011**, *3*, 1562−1567.
(29) Li, S.; Zhang, J.; Kibria, M. G.; Mi, Z.; Chaker, M.; Ma, D.; Nechache, R.; Rosei, F. *Chem. Commun.* **2013**, *49*, 5856−5858.
(30) Luo, W.; Zhu, L.; Wang, N.; Tang, H.; Cao, M.; She, Y. *Environ. Sci. Technol.* **2010**, *44*, 1786−1791.
(31) Huo, Y.; Miao, M.; Zhang, Y.; Zhu, J.; Li, H. *Chem. Commun.* **2011**, *47*, 2089−2091.
(32) Guo, R.; Fang, L.; Dong, W.; Zheng, F.; Shen, M. *J. Phys. Chem. C* **2010**, *114*, 21390−21396.
(33) Ponzoni, C.; Rosa, R.; Cannio, M.; Buscaglia, V.; Finocchio, E.; Nanni, P.; Leonelli, C. *J. Eur. Ceram. Soc.* **2013**, *33*, 1325−1333.
(34) Wang, N.; Zhu, L.; Lei, M.; She, Y.; Cao, M.; Tang, H. *ACS Catal.* **2011**, *1*, 1193−1202.
(35) Li, S.; Lin, Y.-H.; Zhang, B.-P.; Nan, C.-W.; Wang, Y. *J. Appl. Phys.* **2009**, *105*, 056105-1−056105-3.
(36) Li, Z.; Shen, Y.; Yang, C.; Lei, Y.; Guan, Y.; Lin, Y.; Liu, D.; Nan, C. W. *J. Mater. Chem. A* **2013**, *1*, 823−829.
(37) Ji, W.; Yao, K.; Lim, Y.-F.; Liang, Y. C.; Suwardi, A. *Appl. Phys. Lett.* **2013**, *103*, 062901.
(38) Yang, S. Y.; Seidel, J.; Byrnes, S. J.; Shafer, P.; Yang, C. H.; Rossel, M. D.; Yu, P.; Chu, Y. H.; Scott, J. F.; Ager, J. W.; Martin, L. W.; Ramesh, R. *Nature Nano* **2010**, *5*, 143−147.
(39) Alexe, M.; Hesse, D. *Nat. Commun.* **2011**, *2*, 256.
(40) Wu, J.; Zhang, B.; Wang, X. *Appl. Phys. A* **2013**, *111*, 1017−1020.
(41) Dong, H.; Wu, Z.; Wang, S.; Duan, W.; Li, J. *Appl. Phys. Lett.* **2013**, *102*, 072905-1−072905-5.
(42) Zhang, Z.; Yates, J. T. *Chem. Rev.* **2012**, *112*, 5520−5551.
(43) Zhang, Y.; Schultz, A. M.; Salvador, P. A.; Rohrer, G. S. *J. Mater. Chem.* **2011**, *21*, 4168−4174.
(44) Lai, Y.; Sun, L.; Chen, Y.; Zhuang, H.; Lin, C.; Chin, J. W. *J. Electrochem. Soc.* **2006**, *153*, D123−D127.
(45) Thompson, T. L.; Yates, J. T. *Chem. Rev.* **2006**, *106*, 4428−4453.
(46) Zhang, X.; Zhang, L.; Xie, T.; Wang, D. *J. Phys. Chem. C* **2009**, *113*, 7371−7378.
(47) Chang, Y.-H.; Liu, C.-M.; Cheng, H.-E.; Chen, C. *ACS Appl. Mater. Interfaces* **2013**, *5*, 3549−3555.
(48) Ortiz-Quiñonez, J. L.; Díaz, D.; Zumeta-Dubé, I.; Arriola-Santamaría, H.; Betancourt, I.; Santiago-Jacinto, P.; Nava-Etzana, N. *Inorg. Chem.* **2013**, *52*, 10306−10317.
(49) Zhao, Q.; Yu, M.; Xie, T.; Peng, L.; Wang, P.; Wang, D. *Nanotechnology* **2008**, *19*, 245706.
(50) Sikhwivhilu, L. M.; Mpelane, S.; Mwakikunga, B. W.; Sinha Ray, S. *ACS Appl. Mater. Interfaces* **2012**, *4*, 1656−1665.
(51) Shahed, U. M. K.; Mofareh, A. S.; William, B. I., Jr. *Science* **2002**, *297*, 2243−2245.
(52) Zhuang, J.; Dai, W.; Tian, Q.; Li, Z.; Xie, L.; Wang, J.; Liu, P.; Shi, X.; Wang, D. *Langmuir* **2010**, *26*, 9686−9694.
(53) Xu, J.; Wang, W.; Shang, M.; Sun, S.; Ren, J.; Zhang, L. *Appl. Catal., B* **2010**, *93*, 227−232.
(54) Berger, T.; Monllor-Satoca, D.; Jankulovska, M.; Lana-Villarreal, T.; Gómez, R. *ChemPhysChem* **2012**, *13*, 2824−2875.
(55) Zhang, Z.; Yates, J. T. *Chem. Rev.* **2012**, *112*, 5520−5551.
(56) Wang, Y.; Su, Y. R.; Qiao, L.; Liu, L. X.; Su, Q.; Zhu, C. Q.; Liu, X. Q. *Nanotechnology* **2011**, *22*, 225702.
(57) Dong, W.; Guo, Y.; Guo, B.; Li, H.; Liu, H.; Joel, T. W. *ACS Appl. Mater. Interfaces* **2013**, *5*, 6925−6929.
(58) Choi, T.; Lee, S.; Choi, Y. J.; Kiryukhin, V.; Cheong, S. W. *Science* **2009**, *324*, 63−66.
(59) Chen, B.; Li, M.; Liu, Y.; Zuo, Z.; Zhuge, F.; Zhan, Q.-F.; Li, R.-W. *Nanotechnology* **2011**, *22*, 195201.
(60) Wu, F.; Guo, Y.; Guo, B.; Zhang, Y.; Li, H.; Liu, H. *J. Phys. D: Appl. Phys.* **2013**, *46*, 365304.
(61) Li, S.; Morasch, J.; Klein, A.; Chirila, C.; Pintilie, L.; Jia, L.; Ellmer, K.; Naderer, M.; Reichmann, K.; Gröting, M.; Albe, K. *Phys. Rev. B* **2013**, *88*, 045428-1−045428-12.
(62) Yang, J.; Cheng, C. C.; Ji, H. W.; Ma, W. H.; Zhao, J. C. *J. Phys. Chem. B* **2005**, *109*, 21900−21907.
(63) Chen, Y. J.; Huang, R. K.; Chen, D. Q.; Wang, Y. S.; Liu, W. J.; Li, X. N.; Li, Z. H. *ACS Appl. Mater. Interfaces* **2012**, *4*, 2273−2279.
(64) Cheng, M.; Song, W.; Ma, W.; Chen, C.; Zhao, J.; Lin, J.; Zhu, H. *Appl. Catal., B* **2008**, *77*, 355−363.
(65) Qu, P.; Zhao, J.; Shen, T.; Hidaka, H. *J. Mol. Catal. A: Chem.* **1998**, *129*, 257−268.
(66) Ge, S.; Zhang, L. *Environ. Sci. Technol.* **2011**, *45*, 3027−3033.
(67) Lin, D.; Wu, H.; Zhang, R.; Pan, W. *Chem. Mater.* **2009**, *21*, 3479−3484.